



Optical reflectance imaging reveals interlayer coupling in mechanically stacked MoS₂ and WS₂ bilayers

VU NGUYEN,¹ WAN LI,² JOEL AGER,^{3,4} KE XU,²  AND HAYDEN TAYLOR^{1,*} 

¹Department of Mechanical Engineering, University of California, Berkeley, Berkeley, CA 94720, USA

²Department of Chemistry, University of California, Berkeley, Berkeley, CA 94720, USA

³Department of Materials Science and Engineering, University of California, Berkeley, Berkeley, CA 94720, USA

⁴Materials Sciences Division, Lawrence Berkeley National Laboratories, Berkeley, CA 94720, USA

*hkt@berkeley.edu

Abstract: Optical reflectance imaging is a popular technique for characterizing 2D materials, thanks to its simplicity and speed of data acquisition. The use of this method for studying interlayer phenomena in stacked 2D layers has, however, remained limited. Here we demonstrate that optical imaging can reveal the nature of interlayer coupling in stacked MoS₂ and WS₂ bilayers through their observed reflectance contrast versus the substrate. Successful determination of interlayer coupling requires co-optimization of the illumination wavelength and the thickness of an underlying SiO₂ film. Our observations are supported by multilayer optical calculations together with an analysis of the effect of any interlayer gap. This approach promises quick characterization of constructed 2D material systems.

© 2023 Optica Publishing Group under the terms of the [Optica Open Access Publishing Agreement](#)

1. Introduction

Assembly of two-dimensional (2D) material layers through the ubiquitous van der Waals (vdW) force promises to augment bottom-up thin-film manufacturing with access to a wide range of possible material combinations and atomically precise control over out-of-plane composition [1,2]. In this manufacturing approach, molecular monolayers serve as building blocks which have been discovered to exhibit a variety of useful electronic [3,4], optoelectronic [5], and mechanical [6] properties. Such a rich library of components has motivated research in vdW assembly of 2D materials into pre-defined stacks for both fundamental studies and practical applications such as light-emitting diodes [7], photodetectors [8], and tunnel transistors [9]. Conceivably, the interactions between layers in a vdW-assembled stack depend not only on the selection of individual monolayers but also on the interlayer spacing, any interlayer inclusions, and relative crystal orientation [10–17]. Interlayer interactions are typically measured by optical spectroscopy techniques such as photoluminescence (PL) [12,13,17] and Raman spectroscopy [18]. Although such spectroscopic techniques reveal the key optoelectronic characteristics of the stacked 2D layers, they typically characterize only a single point on the material at once, which is slow and unsuitable for quick study of large-area samples. For higher throughput, using a digital camera together with optical microscopy for data acquisition is an attractive approach. This approach has been widely used to determine thicknesses of 2D layers quickly via either comparison with multilayer optical calculations [19–22] or machine learning [23,24], and recently it has also been employed to perform PL imaging, which can visualize interlayer coupling [17]. However, determination of the specific nature of interlayer coupling within 2D heterostructures — and the associated sizes of any inter-layer voids or defects — requires more sensitive detection and modeling of reflectance signals than has previously been deployed. Imaging spectroscopic

ellipsometry (SE) has also been used to visualize the optical properties of 2D monolayers with high spatial resolution [25] and is a promising technique to study stacked 2D materials. Nevertheless, SE still requires specialized apparatus with substantial cost, to which access is likely to be more limited than to standard optical reflectance microscopes of the type used in this work.

In this paper we demonstrate — with mechanically assembled bilayer MoS₂ and WS₂ — that simple optical reflectance imaging can be used not only to identify layer thickness, but also to predict how close the PL response of an assembled bilayer will be to that of a naturally occurring bilayer in commensurate contact. Our technique takes advantage of the subtle thickness dependence of the complex refractive index in transition metal dichalcogenides (TMDCs), a class of vdW solids that has been studied extensively [26–28]. We found that with a suitable combination of illumination wavelength and the thickness of an SiO₂ layer on the substrate, bilayer regions with weak interlayer coupling can yield a starkly different optical reflectance from those with strong interlayer coupling. Here we used the terms “weak” and “strong” coupling in an operational sense, meaning how close the PL of a given bilayer is to that obtained from naturally grown material. We assume that the interlayer coupling is as strong as it can be in a naturally occurring bilayer. We explain the dependence of reflectance on coupling primarily in terms of the subtle thickness-dependence of the complex refractive index of TMDCs, which causes tightly coupled bilayers to behave as a single, thicker, layer and reflect light quite differently from adjacent but less tightly coupled pairs of monolayers.

Several previous studies have investigated the thickness effect on the optical constants [26,29]. For the modeling presented in this work, we used the refractive index data of Hsu *et al.* [26] because the 2D materials reported in that study were exfoliated from similar sources to ours, and a comparable characterization method, microreflection, was used. Other factors such as doping and oxidation may also change the optical response [30], but are unlikely to be prevalent in our experiments and are outside the scope of the current study.

We also identified that the thickness and refractive index of any interlayer matter — such as contaminants from processing — can be manifested in the reflectance signal recorded. Further, we used the imaging technique to explore the ability of thermal annealing of assembled bilayers to increase inter-layer coupling. Our results promise to expand the power of traditional optical microscopy for high-throughput characterization and manufacturing of structures assembled from vdW solids.

2. Materials preparation and experimental setup

Monolayer and stacked bilayer arrays of MoS₂ and WS₂ were fabricated via the Covalent Bond Exfoliate–Align–Release (CoBEARs) process that we have previously reported [31]. Briefly, CoBEARs is based on gold-mediated exfoliation [32,33] and uses a patterned photoresist layer both to mask the etching of the gold film and TMDC layers below, and to serve as a handle for picking up the subsequently exfoliated material. A transparent heat-releasable photoresist tape makes contact with the patterned handle layer to effect material transfer from a source crystal to the target substrate.

Optical reflectance imaging was performed on an Olympus IX73 inverted wide-field epifluorescence microscope equipped with a standard lamp for fluorescence microscopy (U-HGLGPS) [20]. A band-pass filter was applied to the source beam, with one of the following characteristics: 450/10 nm (central wavelength/bandwidth), 532/5 nm, or 610/10 nm (Chroma). When we used the 450 nm or 532 nm illumination, we also used a band-pass filter ET470/40X (Chroma) or ET525/50 m (Chroma), respectively, as an emission filter to prevent any PL emission from reaching the camera. These emission filters are, in practice, optional as we found that the PL signals from our samples are very weak compared to the reflected signals.

The objective lens was an Olympus UPlanSAPO 20× objective (NA 0.5), and it has been shown that for $NA \leq 0.5$, the effect of non-zero incidence angle is negligible [34]. The images were acquired at 16-bit dynamic range using an Andor Zyla 4.2 sCMOS camera at either 1024×1024 pixels or 512×512 pixels and 15 ms integration time. Topography scans were performed with a Park Systems AFM in tapping mode using PPP-NCHR probes.

3. Results and discussion

First, we visualized the contrast difference between the as-fabricated, pre-annealing stacked bilayer MoS₂ and naturally occurring bilayer MoS₂, using images taken with the microscope setup in Fig. 1(a). “Contrast” is defined as the ratio of reflected light intensity from a 2D material region to that from the bare adjacent substrate. A “stacked” bilayer is one that has been constructed manually by sequentially transferring two exfoliated monolayers so that they overlap, but without precisely controlling, for example, the relative angular orientation of the two layers’ atomic lattices. Meanwhile, a “naturally occurring” or “natural” bilayer is exfoliated from the source crystal as two coupled layers in a single CoBEARs step. Even though CoBEARs was developed to exfoliate monolayer material preferentially, the yield is not perfect and sometimes small regions of natural bilayer material are transferred in this way [31,32]. In stacked bilayers that have not yet been annealed, the interlayer coupling is expected to be weak due to the lack of commensurate contact and the possibility of inclusion of impurities between layers [11,31]. The atomic lattices of natural bilayers, meanwhile, are expected to be in commensurate contact, which is evidenced by suppressed PL [5]. After two consecutive depositions of pre-patterned arrays onto a 260 nm SiO₂/Si substrate, as shown in Fig. 1(b–c), regions of both stacked bilayer MoS₂ and naturally occurring bilayer MoS₂ were obtained, highlighted with dashed circles. Under white-light, 610 nm, and 532 nm illumination, the stacked bilayers were almost indistinguishable from the naturally occurring bilayers, as shown in Fig. 1(c–e). However, when we switched to 450 nm illumination, the stacked bilayers were visually brighter than the naturally occurring bilayers, as shown in Fig. 1(f). One might initially imagine that this difference was caused by the expected weaker coupling between the component monolayers of a stacked bilayer, and the far greater PL intensity of uncoupled monolayers of MoS₂ compared to a well-coupled natural bilayer or thicker material [17]. However, we showed that the higher reflectance contrast of the stacked bilayers was not in fact due to PL of overlapped and uncoupled monolayers, because when inserting an emission filter to exclude the PL peak of monolayer MoS₂ at ~670 nm from the received signal, we obtained similar reflectance contrast. This showed that the PL signal in our samples is much weaker than the reflected signal, so having this emission filter in our case is, in practice, optional.

The substrate plays an important role, since when we fabricated stacked bilayer MoS₂ on a 285 nm SiO₂/Si substrate (as opposed to 260 nm; see Fig. 7), such an obvious contrast difference was no longer observed under any of the 610 nm, 532 nm, and 450 nm illumination wavelengths. This result highlights the importance of co-optimizing the illumination wavelength and substrate composition for making sensitive observations, as we will examine in more detail later in this paper. At our selected imaging conditions — 450 nm illumination and 260 nm SiO₂/Si substrate — we show below that the pronounced difference between stacked and natural bilayer contrast is in large part due to the influence of interlayer coupling on light reflection, and to a lesser extent due to interlayer materials.

To understand our observations in Fig. 1, we used Fresnel’s equations and the transfer matrix method [20,21] to simulate the reflectance contrast between the multilayered vdW material and the surrounding bare SiO₂/Si substrate for the scheme in Fig. 2(a). For the initial simulation results shown in Fig. 2, all gaps between layers were set to be zero-thickness. Values for thickness-dependent complex refractive indices of TMDCs (Fig. 5(e)–(f)) were taken from published results [26], which were obtained using the micro-reflectance method for 2D layers on

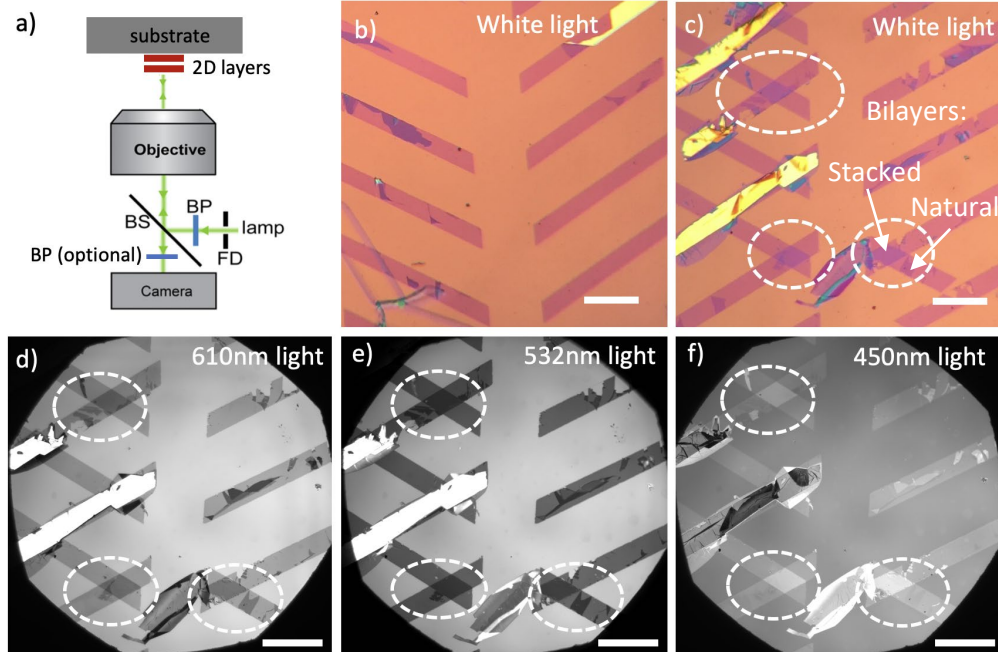


Fig. 1. Comparison of the reflectance images of pre-annealing stacked and naturally occurring bilayers of MoS₂ on a 260 nm SiO₂/Si substrate. (a) Schematic of the microscope setup. FD: field diaphragm, BP: band-pass filter, BS: beam splitter. (b) White-light reflectance image of an array of monolayer regions after one MoS₂ transfer step. Multilayer regions occasionally occur due to imperfect monolayer yield of the CoBEARs process. (c) White-light reflectance image showing diamond-shaped stacked bilayer regions at the intersections of overlapping monolayer sheets transferred by two consecutive CoBEARs processes. (d–f) The same sample as in (c) but under 610 nm, 532 nm, and 450 nm illumination, respectively. Scale bars are 100 μm.

silicon wafers with different SiO₂ thicknesses. For the bilayer case, we carried out simulations under two alternative assumptions for the refractive index of the TMDC: one that each TMDC layer had the refractive index of an independent monolayer, and the other that the TMDC layers were effectively coupled and took on the refractive index of two-layer-thick material. Plots of modeled and experimental contrast results for monolayers, natural bilayers, and pre-annealing stacked bilayers are shown in Fig. 2(b–d) for three distinct optical wavelengths: 610 nm, 532 nm and 450 nm. These results agree with the observations in Fig. 1(d–f), and strongly suggest that in terms of complex refractive index, the pre-annealing stacked bilayer regions in Fig. 1(f) behave as if they consist of two uncoupled monolayers. This finding is particularly clear in Fig. 2(d), where the simulation assuming the TMDC refractive index to equal that of an isolated monolayer (dashed line) closely matches the experimental contrast results for the stacked (mechanically assembled) bilayer, whereas the simulation assuming the bilayer TMDC refractive index (solid line) closely matches the experimental results for the natural bilayers.

The simulations again highlight the importance of selecting suitable illumination wavelengths for a given substrate to enhance the contrast difference between the weak and strong interlayer coupling. In this case, 450 nm is more suitable than 610 nm and 532 nm when used in conjunction with a 260 nm SiO₂/Si substrate. We study a wider range of wavelengths and SiO₂ thicknesses later in the text.

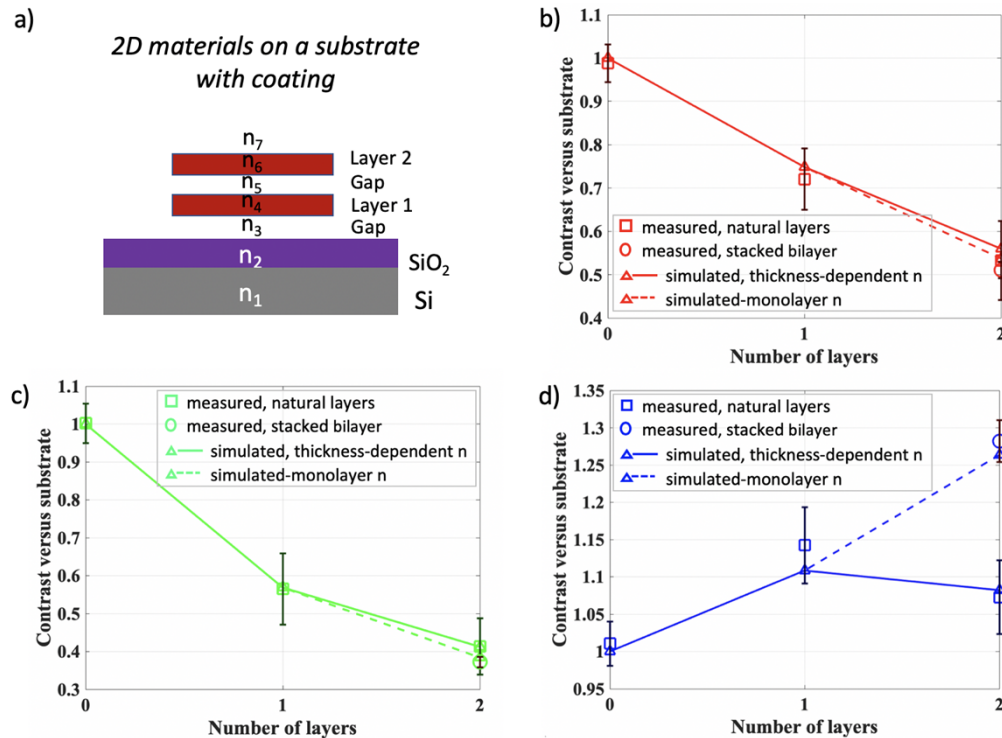


Fig. 2. Simulation of the reflectance contrasts of 2D bilayers versus a bare 260 nm SiO_2/Si substrate using the well-known Fresnel's equations and transfer matrix method. (a) Multilayer model for up to two 2D layers with intermediate gaps. The top medium (labeled n_7) is air. The role played by intermediate gaps is ignored in this figure but is included later in the paper. Simulated versus measured contrast values are plotted for (b) 610 nm, (c) 532 nm and (d) 450 nm sample illumination, respectively. Error bars indicate \pm three standard deviations of the contrast extracted from all pixels in the image containing the corresponding number of layers.

The ability to distinguish between two levels of interlayer coupling for bilayer MoS_2 prompted us also to study post-annealing stacked bilayers, as annealing has previously been shown to be able to displace interlayer contaminants and, thus, modify the interlayer coupling [11,35,36]. Annealing was carried out by exposing the samples to 200 °C heat on a hotplate for five minutes. Since we conducted the annealing in air, we chose a relatively short annealing time to minimize any oxidation of our materials, which can be expected to be much smaller than 15% by mass based on previous work [30]. Surface roughness (Fig. 3(e)) and PL spectra (Fig. 3(c)) of post-annealing material show no noticeable changes from freshly exfoliated, unannealed material. Thus, we assumed that any oxidation-induced change in the optical properties of our 2D materials is sufficiently small, and we excluded this effect in our subsequent simulations. Figure 3(a) shows a region of post-annealed stacked bilayer MoS_2 on 260 nm SiO_2/Si substrate, fabricated by placing a randomly shaped monolayer on top of a $100 \times 100 \mu\text{m}^2$ monolayer. Again, the imperfect monolayer yield of the exfoliation gave us an area of naturally occurring bilayer material next to the square area of the stacked bilayer, against which the annealed, stacked material can be referenced. The colored dots in Fig. 3(a) in conjunction with the legend in Fig. 3(c) identify the different types of material in the image.

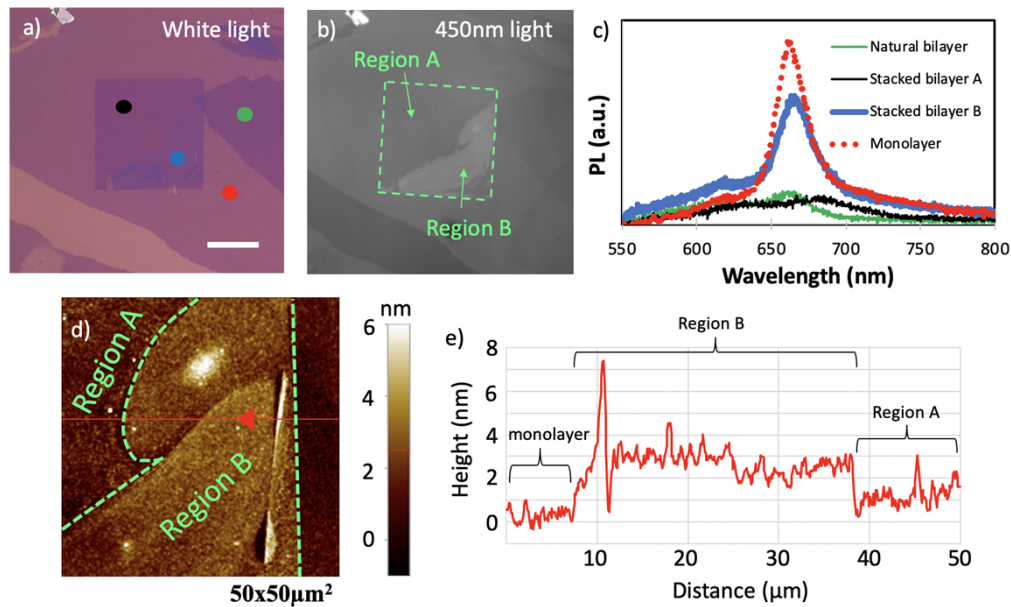


Fig. 3. Contrast, interlayer coupling and topography in a post-annealing stacked bilayer. (a) White-light image of a square stacked bilayer region with a nearby naturally occurring bilayer on a 260 nm SiO₂/Si substrate. Scale bar is 50 μm. (b) Image of the sample in (a) under 450 nm monochrome illumination. The square is divided into region A of lower contrast and region B of higher contrast. (c) PL spectra of the color-coded points in (a). (d) AFM topography scan, whose cross-section at the red line is shown in (e).

There is some evidence under white light (Fig. 3(a)) of color heterogeneity within the $100 \times 100 \mu\text{m}^2$ stacked bilayer region, possibly due to the presence of localized inter-layer contamination [35,36], which most likely is air and/or water molecules as the stacking was conducted in ambient conditions [31]. By switching to 450 nm illumination, we can more clearly discern two distinct regions within the stacked bilayer, a darker region A and a brighter region B, as shown in Fig. 3(b). Results from Fig. 2 for the previous sample suggest that region A exhibits stronger interlayer coupling than region B, which is verified by the much stronger PL signal found in region B than in region A (Fig. 3(c)). Meanwhile, the red and green traces in Fig. 3(c) show the expected prominent and quenched PL peaks for regions of monolayer and naturally occurring bilayer material, respectively.

Since interlayer coupling is influenced by the interlayer vdW distance [11,12], we acquired an AFM topography scan of the two regions, which is shown in Fig. 3(d) with a cross-section in Fig. 3(e). The AFM topography indicates that the interlayer vdW distance in region B is about 1–2 nm — or even in some places 5 nm — larger than that of region A, which is consistent with the reflectance contrast and PL measurements. Although the measured magnitudes of the step heights distinguishing the regions may be mildly affected by, *e.g.*, charge accumulation during the AFM scanning process, the considerably greater thickness of region B compared to the other regions — and of region A compared to the monolayer — is clear and consistent. It is possible that an accumulation of interlayer materials — or wrinkling of the upper monolayer — increased the separation between the two monolayers in region B, and thus weakened their coupling. In a production process, sensitive optical reflectance imaging as illustrated in Fig. 3(b) could be used quickly to identify regions of post-annealing stacked bilayer material with defective morphology and weak interlayer coupling.

In the simulations discussed so far, the observed differences in reflectance contrast between pre-annealing constructed bilayers and natural or annealed ones were well captured simply by modulating the assumed refractive index of the MoS₂ material. The index was assigned its literature bilayer or monolayer value [26] according to whether or not the two layers were assumed to be tightly optoelectronically coupled. In all those simulations, the two MoS₂ layers were modeled without any intervening gap. However, AFM scans suggest that measurable separations can exist between two assembled layers. This observation could explain the modest discrepancies between measured and simulated reflectance contrast values in Fig. 2.

To refine the reflectance simulations, we explored how the deviations between modeled and measured optical reflectances varied when the effect of interlayer gaps was explicitly included. We explored the influence of gap size and the refractive index of the matter within it. From the AFM topography in Fig. 3(d–e), we estimated the range of possible gap sizes as 0–5 nm. We considered real refractive indices of 1–1.7, to encompass possible inter-layer materials from air to water to organic contaminants. This deviation, or error, between the modeled and measured optical reflectances is then defined as:

$$\text{error} = |C(t_g, n_g) - C_{\text{mean}}|$$

where $C(t_g, n_g)$ is the contrast of the layer of interest as a function of gap thickness t_g and its real refractive index n_g , and C_{mean} is the mean value of measured contrast of the layer of interest.

First, we simulated the influence of a gap between the SiO₂ substrate coating and the lower MoS₂ layer (the gap labeled n_3 in Fig. 2(a)). The results in Fig. 4(b) show that the deviation between the simulated and measured reflectance contrasts at 450 nm illumination was minimized for a gap of 3 nm and refractive index 1.2, which may represent trapped air and water molecules. These values for the MoS₂–SiO₂ gap were used in subsequent simulations.

We then studied the effect of the gap parameters between the two MoS₂ layers (the gap labeled n_5 in Fig. 2(a)). First, we considered region A of the stacked bilayer as shown in Figs. 3(b) and 4(a), where the layers are believed to be relatively close and well coupled. As found earlier, the deviations between measured and simulated reflectance contrast were considerably lower when the MoS₂ was modeled with the literature value for the refractive index of bilayer material than when the monolayer refractive index was assumed (the cases named “2xhalfbilayers” and “2xmonolayers” respectively, in Fig. 4(c–d)). Now, though, we simulated splitting the bilayer material into two halves of equal thickness and inserting a gap of variable thickness and index between them to explore how the modeled reflectance changed. The pseudocolor plot in Fig. 4(c) suggests that modeling error is minimized for a small finite interlayer gap distance (e.g. 2 nm at index of 1.2), rather than for a zero gap distance. However, the error is well below 0.05 even when any interlayer gap is ignored, which is considerably smaller than the difference in contrast between regions A and B that this method is seeking to detect.

Meanwhile, in region B, where AFM had confirmed that the layers were likely separated by a few nanometers, simulation errors were — in agreement with Fig. 2(d) — much smaller when the MoS₂ index was assumed to take on its monolayer value (Fig. 4(f)) than its bilayer value (Fig. 4(e)). Again, simulation error was minimized for a small finite inter-layer gap, but residuals even for zero assumed gap size were much smaller than the contrast differences between regions A and B. It does not therefore appear to be necessary to model inter-layer gaps explicitly to distinguish between MoS₂ bilayers with differing degrees of optoelectronic coupling.

Next, we explore co-optimization of the illumination wavelength and the SiO₂ thickness to reveal the extent of inter-layer coupling most strongly. For highly sensitive detection, we desire the largest possible difference between the magnitudes of reflectance contrast arising from closely (“2xhalfbilayers”) and loosely (“2xmonolayers”) coupled bilayers. Figures 5(a) and 5(b) map this contrast difference for MoS₂ and WS₂ bilayers, respectively, against illumination wavelength and SiO₂ thickness. Several desirable regions of high contrast difference can be identified

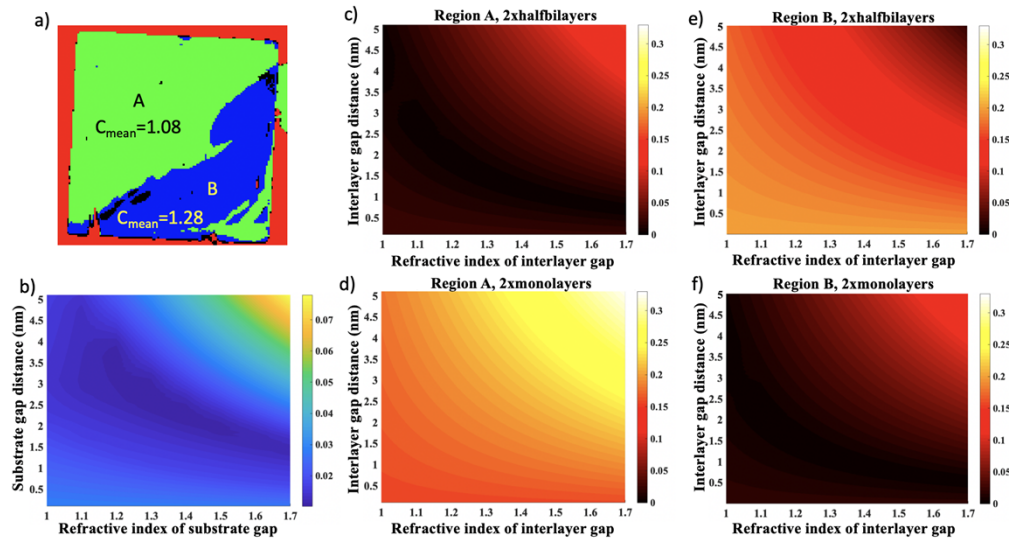


Fig. 4. Error between simulated reflectance contrast and mean measured contrasts for regions A and B, at 450 nm illumination as a function of assumed gap parameters. (a) Labeled map of three regions: monolayer MoS₂ (red), "2xhalfbilayers" region (green) and "2xmonolayers" region (blue). Black pixels indicate unrecognized regions. (b) Error as a function of gap with substrate, averaged across regions of naturally occurring bilayer and monolayer material in sample (a). (c–f) Error of stacked bilayer contrast as a function of interlayer gap parameters, when "2xhalfbilayers" and "2xmonolayers" models are applied to regions A and B, respectively.

readily. Figures 5(c) and 5(d) show the contrast difference figures of merit against illumination wavelength for the specific SiO₂ thickness of 260 nm used experimentally in this work. The three vertical dashed lines in each plot indicate the filter wavelengths we used in this paper: 450 nm, 532 nm and 610 nm. Figure 5(c) is consistent with Fig. 1(d–f) in that the 450 nm illumination wavelength yields the best contrast between the strongly and weakly coupled bilayers. Figure 5(d) also suggests the same scenario for the imaging of WS₂ bilayers. The wavelength-dependent complex refractive indices obtained from Hsu *et al.* [26] are replotted in Fig. 5(e–f) for MoS₂ and WS₂, respectively. These n and k dispersions were fitted by Hsu *et al.* [26] from reflectance data, and, as those authors point out, in specific parts of spectrum could contain substantial uncertainty due to measurement error and collinearity of the fitting parameters. However, our experimental results, which were obtained at 450 nm, 532 nm and 610 nm, are outside of the potentially anomalous regions of the spectra reported by Hsu *et al.* [26]. Comparison between Fig. 5(c–d) and Fig. 5(e–f) further highlights that the highest contrast between 2xhalfbilayers and 2xmonolayers is the result of the co-optimization between illumination wavelength and the substrate composition, and selecting the wavelength alone based on Fig. 5(e–f) may not be sufficient. Figure 6 and Fig. 7 confirm experimentally our simulation results in Fig. 5(a–d).

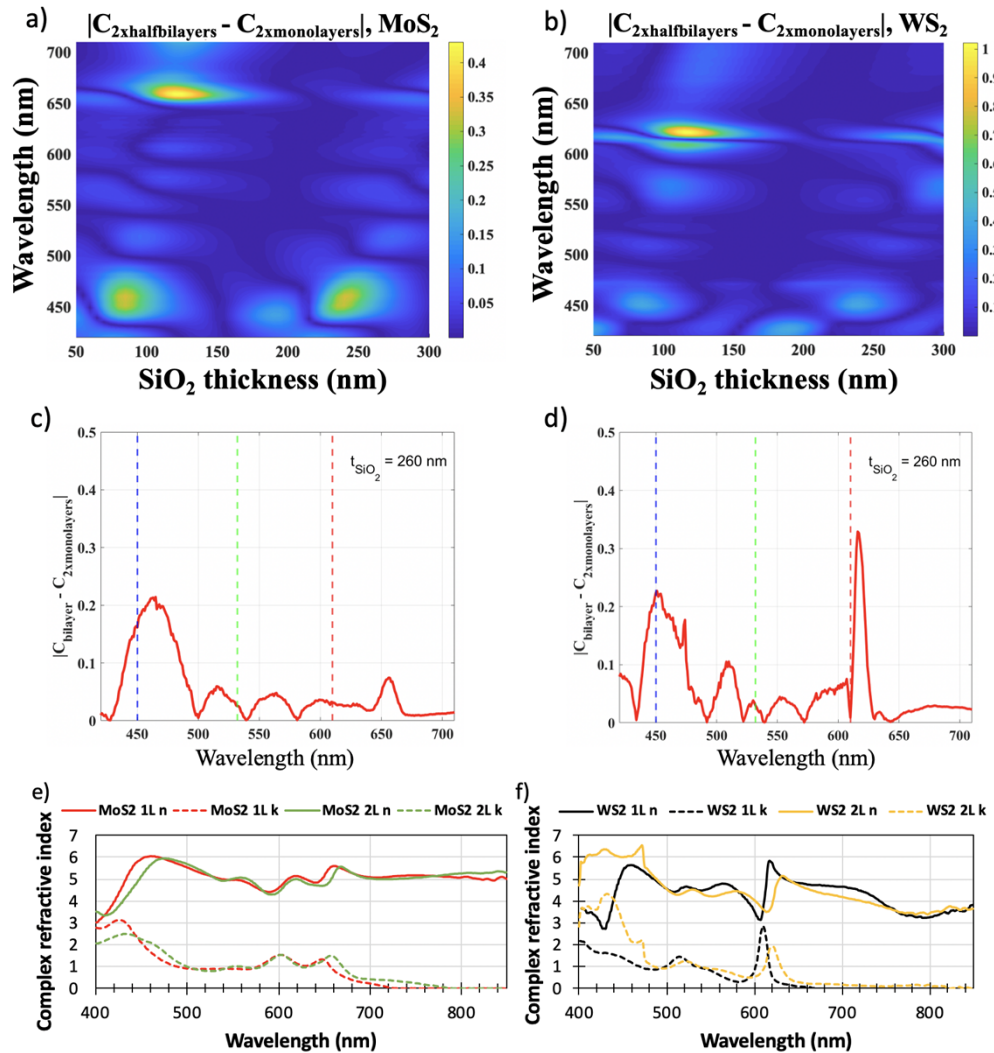


Fig. 5. Impact of the choice of illumination wavelength and SiO₂ thickness of the substrate on the contrast difference between weakly coupled and strongly coupled stacked bilayers. Simulated contrast difference for bilayer MoS₂ in (a) and WS₂ in (b). (c) Simulated contrast difference versus illumination wavelength for bilayer MoS₂ on 260 nm SiO₂/Si. (d) Simulated contrast difference versus illumination wavelength for bilayer WS₂ on 260 nm SiO₂/Si. (e–f) Complex refractive indices of monolayer and bilayer MoS₂ and WS₂, respectively, replotted from Hsu et al. [26] used in all the simulations in this work. (*n* is the real component and *k* the imaginary component of refractive index.)

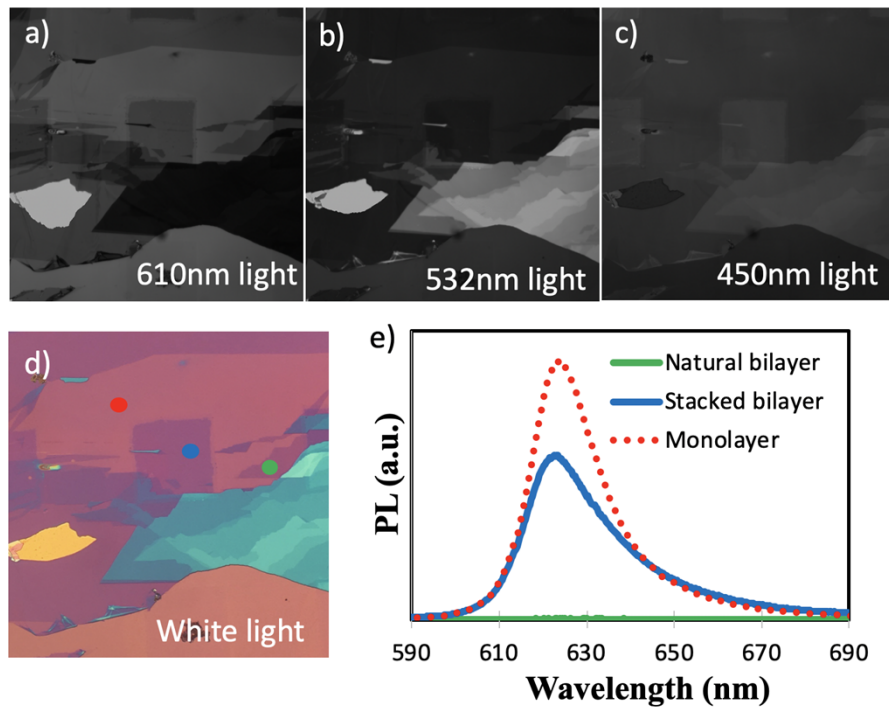


Fig. 6. Comparison of contrasts of WS₂ stacked bilayer and naturally occurring bilayer on 260 nm SiO₂/Si substrate, which is consistent with the result in Fig. 5(d). The illumination wavelengths in (a–c) are 610 nm, 532 nm, and 450 nm, respectively. (d) The sample under white light illumination labeled with red (monolayer), green (natural bilayer) and blue (stacked bilayer) spots where PL spectra were obtained. (e) PL spectra of the color-coded spots in (d), showing the corresponding weak (prominent peak) and strong (no peak) interlayer coupling. As with MoS₂, only the 450 nm illumination clearly distinguishes between the natural and stacked bilayer material through reflectance imaging.

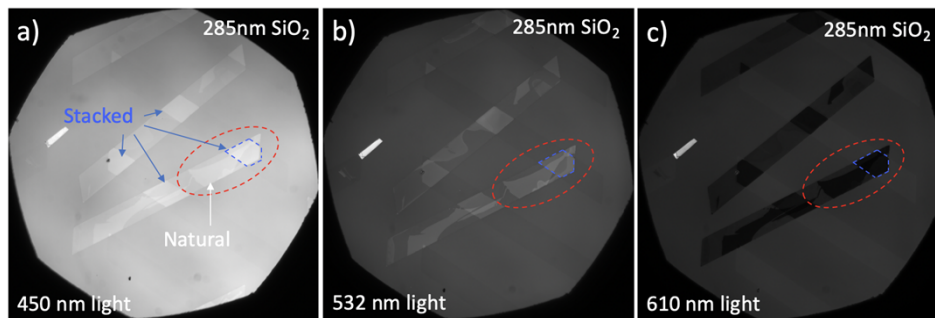


Fig. 7. Comparison of contrasts of MoS₂ stacked bilayer and naturally occurring bilayer on 285 nm SiO₂/Si substrate. The illumination wavelengths in (a–c) are 450 nm, 532 nm, and 610 nm, respectively. In agreement with Fig. 5(a), compared to 450 nm wavelength and 260 nm SiO₂ thickness, such as in Fig. 1(f), 450 nm wavelength and 285 nm SiO₂ thickness, as in (a), results in lower contrast difference between 2xhalfbilayer and 2xmonolayer at 450 nm illumination wavelength.

4. Concluding remarks

We have shown through the study of stacked bilayer MoS₂ and WS₂ that by selecting a suitable combination of illumination wavelength with the thickness of an SiO₂ film on the substrate, a clear difference can be realized between the optical reflectance contrasts of weakly and strongly coupled bilayer regions. This clear difference between optical reflectance values can be mainly attributed to the thickness-dependence of the complex refractive index of the vdW bilayers. Other factors that can change the complex refractive index such as oxidation and doping were ignored in our study, and could be a subject of future investigation for a more comprehensive treatment. Strongly coupled bilayers — which occur in natural material or can be obtained by thermally annealing a mechanically assembled bilayer — exhibit a different effective refractive index from bilayers that are weakly coupled. Bilayers may be weakly coupled if they have been mechanically assembled by repeated exfoliation steps but not annealed. Bilayers may also remain weakly coupled even after thermal annealing if there is some residual imperfection such as inter-layer contamination or wrinkling. The sizes and contents of any nanometer-level inter-layer gaps have a much smaller effect on optical reflectance than the effective refractive index of the vdW layers themselves.

The results of our study show that optical reflectance imaging could be a powerful tool to quickly characterize interlayer coupling, highlight locations of possible interlayer contamination, and identify layer thickness in the nanomanufacturing of 2D materials.

Funding. Bakar Fellows Award; Basic Energy Sciences (DE-AC02-05CH11231); National Science Foundation (1636256, 1720701, DMR 1548924, EEC-1160494).

Acknowledgements. The authors thank Daryl Chrzan for insightful discussions throughout this work on the exfoliation and transfer of monolayers as well as on the characterization of the constructed bilayers. The nanofabrication was supported by the National Science Foundation, Award 1636256: SNM: Scalable Nano-manufacturing of 2D Electronic Materials and Devices Using Automated Exfoliation, and by National Science Foundation Cooperative Agreement No. EEC-1160494 (NASCENT). Software development was supported by the National Science Foundation, Award 1720701: Network for Computational Nanotechnology – Hierarchical NanoMFG Node. Photoluminescence characterization was supported by the Electronic Materials Program, funded by the Director, Office of Science, Office of Basic Energy Sciences, Materials Sciences and Engineering Division of the U.S. Department of Energy, under Contract DE-AC02-05CH11231. Optical reflectance imaging was supported by STROBE, a National Science Foundation Science and Technology Center under Grant No. DMR 1548924, and the Bakar Fellows Award. The 2D materials fabrication was achieved thanks to access to the facilities at the Biomolecular Nanotechnology Center (BNC) of the California Institute for Quantitative Biosciences (QB3), and the Berkeley Marvell NanoLab.

Disclosures. The authors declare no conflicts of interest.

Data Availability. Data underlying the results presented in this paper are not publicly available at this time but may be obtained from the authors upon reasonable request.

References

1. A. K. Geim and I. V. Grigorieva, “Van der Waals heterostructures,” *Nature* **499**(7459), 419–425 (2013).
2. Y. Liu, Y. Huang, and X. Duan, “Van der Waals integration before and beyond two-dimensional materials,” *Nature* **567**(7748), 323–333 (2019).
3. K. S. Novoselov, A. K. Geim, S. V. Morozov, D. Jiang, Y. Zhang, S. V. Dubonos, I. V. Grigorieva, and A. A. Firsov, “Electric field effect in atomically thin carbon films,” *Science* **306**(5696), 666–669 (2004).
4. B. Radisavljevic, A. Radenovic, J. Brivio, V. Giacometti, and A. Kis, “Single-layer MoS₂ transistors,” *Nat. Nanotechnol.* **6**(3), 147–150 (2011).
5. K. F. Mak, C. Lee, J. Hone, J. Shan, and T. F. Heinz, “Atomically thin MoS₂: A new direct-gap semiconductor,” *Phys. Rev. Lett.* **105**(13), 136805 (2010).
6. S. Bertolazzi, J. Brivio, and A. Kis, “Stretching and breaking of ultrathin MoS₂,” *ACS Nano* **5**(12), 9703–9709 (2011).
7. F. Withers, O. Del Pozo-Zamudio, A. Mishchenko, A. P. Rooney, A. Gholinia, K. Watanabe, T. Taniguchi, S. J. Haigh, A. K. Geim, A. I. Tartakovskii, and K. S. Novoselov, “Light-emitting diodes by band-structure engineering in van der Waals heterostructures,” *Nat. Mater.* **14**(3), 301–306 (2015).
8. K. Zhang, T. Zhang, G. Cheng, T. Li, S. Wang, W. Wei, X. Zhou, W. Yu, Y. Sun, P. Wang, D. Zhang, C. Zeng, X. Wang, W. Hu, H. J. Fan, G. Shen, X. Chen, X. Duan, K. Chang, and N. Dai, “Interlayer Transition and Infrared Photodetection in Atomically Thin Type-II MoTe₂/MoS₂ van der Waals Heterostructures,” *ACS Nano* **10**(3), 3852–3858 (2016).

9. T. Roy, M. Tosun, X. Cao, H. Fang, D. H. Lien, P. Zhao, Y. Z. Chen, Y. L. Chueh, J. Guo, and A. Javey, "Dual-gated MoS₂/WSe₂ van der Waals tunnel diodes and transistors," *ACS Nano* **9**(2), 2071–2079 (2015).
10. K. Kang, K. H. Lee, Y. Han, H. Gao, S. Xie, D. A. Muller, and J. Park, "Layer-by-layer assembly of two-dimensional materials into wafer-scale heterostructures," *Nature* **550**(7675), 229–233 (2017).
11. S. Tongay, W. Fan, J. Kang, J. Park, U. Koldemir, J. Suh, D. S. Narang, K. Liu, J. Ji, J. Li, R. Sinclair, and J. Wu, "Tuning interlayer coupling in large-area heterostructures with CVD-grown MoS₂ and WS₂ monolayers," *Nano Lett.* **14**(6), 3185–3190 (2014).
12. W. Xu, D. Kozawa, Y. Liu, Y. Sheng, K. Wei, V. B. Koman, S. Wang, X. Wang, T. Jiang, M. S. Strano, and J. H. Warner, "Determining the Optimized Interlayer Separation Distance in Vertical Stacked 2D WS₂:hBN:MoS₂ Heterostructures for Exciton Energy Transfer," *Small* **14**(13), 1703727 (2018).
13. S. Huang, X. Ling, L. Liang, J. Kong, H. Terrones, V. Meunier, and M. S. Dresselhaus, "Probing the interlayer coupling of twisted bilayer MoS₂ using photoluminescence spectroscopy," *Nano Lett.* **14**(10), 5500–5508 (2014).
14. K. Liu, L. Zhang, T. Cao, C. Jin, D. Qiu, Q. Zhou, A. Zettl, P. Yang, S. G. Louie, and F. Wang, "Evolution of interlayer coupling in twisted molybdenum disulfide bilayers," *Nat. Commun.* **5**(1), 4966 (2014).
15. Y. Gong, J. Lin, X. Wang, G. Shi, S. Lei, Z. Lin, X. Zou, G. Ye, R. Vajtai, B. I. Yakobson, H. Terrones, M. Terrones, B. K. Tay, J. Lou, S. T. Pantelides, Z. Liu, W. Zhou, and P. M. Ajayan, "Vertical and in-plane heterostructures from WS₂/MoS₂ monolayers," *Nat. Mater.* **13**(12), 1135–1142 (2014).
16. H. Fang, C. Battaglia, C. Carraro, S. Nemsak, B. Ozdol, J. S. Kang, H. A. Bechtel, S. B. Desai, F. Kronast, A. A. Unal, G. Conti, C. Conlon, G. K. Palsson, M. C. Martin, A. M. Minor, C. S. Fadley, E. Yablonovitch, R. Maboudian, and A. Javey, "Strong interlayer coupling in van der Waals heterostructures built from single-layer chalcogenides," *Proc. Natl. Acad. Sci. U.S.A.* **111**(17), 6198–6202 (2014).
17. E. M. Alexeev, A. Catanzaro, O. V. Skrypka, P. K. Nayak, S. Ahn, S. Pak, J. Lee, J. I. Sohn, K. S. Novoselov, H. S. Shin, and A. I. Tartakovskii, "Imaging of Interlayer Coupling in van der Waals Heterostructures Using a Bright-Field Optical Microscope," *Nano Lett.* **17**(9), 5342–5349 (2017).
18. S. Huang, L. Liang, X. Ling, A. A. Puretzy, D. B. Geohegan, B. G. Sumpter, J. Kong, V. Meunier, and M. S. Dresselhaus, "Low-Frequency Interlayer Raman Modes to Probe Interface of Twisted Bilayer MoS₂," *Nano Lett.* **16**(2), 1435–1444 (2016).
19. Z. H. Ni, H. M. Wang, J. Kasim, H. M. Fan, T. Yu, Y. H. Wu, Y. P. Feng, and Z. X. Shen, "Graphene thickness determination using reflection and contrast spectroscopy," *Nano Lett.* **7**(9), 2758–2763 (2007).
20. W. Li, S. Moon, M. Wojcik, and K. Xu, "Direct Optical Visualization of Graphene and Its Nanoscale Defects on Transparent Substrates," *Nano Lett.* **16**(8), 5027–5031 (2016).
21. C. Casiraghi, A. Hartschuh, E. Lidorikis, H. Qian, H. Harutyunyan, T. Gokus, K. S. Novoselov, and A. C. Ferrari, "Rayleigh imaging of graphene and graphene layers," *Nano Lett.* **7**(9), 2711–2717 (2007).
22. M. M. Benameur, B. Radisavljevic, J. S. Héron, S. Sahoo, H. Berger, and A. Kis, "Visibility of dichalcogenide nanolayers," *Nanotechnology* **22**(12), 125706 (2011).
23. S. Masubuchi and T. Machida, "Classifying optical microscope images of exfoliated graphene flakes by data-driven machine learning," *npj 2D Mater. Appl.* **3**(1), 4–6 (2019).
24. X. Lin, Z. Si, W. Fu, J. Yang, S. Guo, Y. Cao, J. Zhang, X. Wang, P. Liu, K. Jiang, and W. Zhao, "Intelligent identification of two-dimensional nanostructures by machine-learning optical microscopy," *Nano Res.* **11**(12), 6316–6324 (2018).
25. M. Magnozzi, T. Pflug, M. Ferrera, S. Pace, L. Ramó, M. Olbrich, P. Canepa, H. Ağircan, A. Horn, S. Forti, O. Cavalleri, C. Coletti, F. Bisio, and M. Canepa, "Local Optical Properties in CVD-Grown Monolayer WS₂ Flakes," *J. Phys. Chem. C* **125**(29), 16059–16065 (2021).
26. C. Hsu, R. Frisenda, R. Schmidt, A. Arora, S. M. de Vasconcellos, R. Bratschitsch, H. S. J. van der Zant, and A. Castellanos-Gomez, "Thickness-Dependent Refractive Index of 1 L, 2 L, and 3 L MoS₂, MoSe₂, WS₂, and WSe₂," *Adv. Optical Mater.* **7**(13), 1900239 (2019).
27. B. Song, H. Gu, M. Fang, X. Chen, H. Jiang, R. Wang, T. Zhai, Y. T. Ho, and S. Liu, "Layer-Dependent Dielectric Function of Wafer-Scale 2D MoS₂," *Adv. Opt. Mater.* **7**(2), 1801250 (2019).
28. S. Funke, B. Miller, E. Parzinger, P. Thiesen, A. W. Holleitner, and U. Wurstbauer, "Imaging spectroscopic ellipsometry of MoS₂," *J. Phys.: Condens. Matter* **28**(38), 385301 (2016).
29. Y. Yu, Y. Yu, Y. Cai, W. Li, A. Gurarslan, H. Peelaers, D. E. Aspnes, C. G. Van de Walle, N. V. Nguyen, Y.-W. Zhang, and L. Cao, "Exciton-dominated Dielectric Function of Atomically Thin MoS₂ Films," *Sci. Rep.* **5**(1), 16996 (2015).
30. P. R. Stevenson, R. T. Busch, R. Torsi, A. M. Jawaid, R. Rao, D. B. Lioi, J. A. Robinson, N. R. Glavin, R. A. Vaia, W. J. Kennedy, and J. P. Vernon, "Reversibly Tailoring Optical Constants of Monolayer Transition Metal Dichalcogenide MoS₂ Films: Impact of Dopant-Induced Screening from Chemical Adsorbates and Mild Film Degradation," *ACS Photonics* **8**(6), 1705–1717 (2021).
31. V. Nguyen, H. Gramling, C. Towle, W. Li, D.-H. Lien, H. Kim, D. C. Chrzan, A. Javey, K. Xu, J. Ager, and H. Taylor, "Deterministic Assembly of Arrays of Lithographically Defined WS₂ and MoS₂ Monolayer Features Directly From Multilayer Sources Into Van Der Waals Heterostructures," *J. Micro Nano-Manuf.* **7**(4), 1–8 (2019).
32. H. M. Gramling, C. M. Towle, S. B. Desai, H. Sun, E. C. Lewis, V. D. Nguyen, J. W. Ager, D. Chrzan, E. M. Yeatman, A. Javey, and H. Taylor, "Spatially Precise Transfer of Patterned Monolayer WS₂ and MoS₂ with Features Larger than 10 μm^2 Directly from Multilayer Sources," *ACS Appl. Electron. Mater.* **1**(3), 407–416 (2019).

33. S. B. Desai, S. R. Madhvapathy, M. Amani, D. Kiriya, M. Hettick, M. Tosun, Y. Zhou, M. Dubey, J. W. Ager, D. Chrzan, and A. Javey, "Gold-Mediated Exfoliation of Ultralarge Optoelectronically-Perfect Monolayers," *Adv. Mater.* **28**(21), 4053–4058 (2016).
34. H. Zhang, Y. Ma, Y. Wan, X. Rong, Z. Xie, W. Wang, and L. Dai, "Measuring the Refractive Index of Highly Crystalline Monolayer MoS₂ with High Confidence," *Sci. Rep.* **5**(1), 8440 (2015).
35. A. Jain, P. Bharadwaj, S. Heeg, M. Parzefall, T. Taniguchi, K. Watanabe, and L. Novotny, "Minimizing residues and strain in 2D materials transferred from PDMS," *Nanotechnology* **29**(26), 265203 (2018).
36. D. G. Purdie, N. M. Pugno, T. Taniguchi, K. Watanabe, A. C. Ferrari, and A. Lombardo, "Cleaning interfaces in layered materials heterostructures," *Nat. Commun.* **9**(1), 5387 (2018).